Supplementary Materials For:

Quenched excitons in WSe_2/α-$RuCl_3$ heterostructures revealed by multi-messenger nanoscopy

Aaron J. Sternbach[1†*], Rocco A. Vitalone[1*], Sara Shabani[1*], Jin Zhang[2*], Thomas P. Darlington[3], Samuel L. Moore[1], Sang Hoon Chae[3,‡], Eric Seewald[1], Xiaodong Xu[4], Cory R. Dean[1], Xiaoyang Zhu[5], Angel Rubio[2,6], James Hone[3], Abhay N. Pasupathy[1], P. James Schuck[3] and D. N. Basov[1]

* These authors contributed equally to this work

[1] *Department of Physics, Columbia University, New York, NY 10027, USA*
[2] *Max Planck Institute for the Structure and Dynamics of Matter, Luruper Chaussee 149, 22761 Hamburg, Germany*
[3] *Department of Mechanical Engineering, Columbia University, New York, NY 10027, USA*
[4] *Department of Physics, University of Washington, Seattle, WA 98195, USA*
[5] *Department of Chemistry, Columbia University, New York, NY 10027, USA*
[6] *Center for Computational Quantum Physics (CCQ), Flatiron Institute, 162 Fifth Avenue, New York, NY 10010, USA*

‡ Present address: School of Electrical and Electronic Engineering, School of Materials Science and Engineering, Nanyang Technological University, Singapore 639798, Singapore

†Corresponding author. email as5049@columbia.edu

Section S1.1 – Near-field Spectroscopy

Near-field scattering amplitude, S_{norm}, spectra obtained on monolayer WSe_2 are shown with the black curves in panels (a) and (b) of Fig. S1. The scattering amplitude observed on WSe_2 is slightly higher than the SiO_2 substrate at THz to mid-infrared frequencies (Fig. S1a). In the visible range the near-field amplitude displays a prominent edge near the frequency where a maximum is observed in the visible near-field phase spectra in Fig. 3a and 4b of the main text. We remark that both of these features are consistent with the spectral features reported in Ref [1], which arise from the A-exciton.

Near-field spectra were also collected on the $WSe_2/RuCl_3$ heterostructure at THz to Visible frequencies shown in panels (c) and (d) of Fig. S1. Spectra of S_{norm} show enhanced scattering at THz frequencies and suppressed scattering at Mid-infrared frequencies as discussed in the main text. In the visible range, deviations from a featureless spectral response are indistinguishable from noise consistent with the suppressed A-exciton resonance observed in the phase and PL data, discussed in the main text.

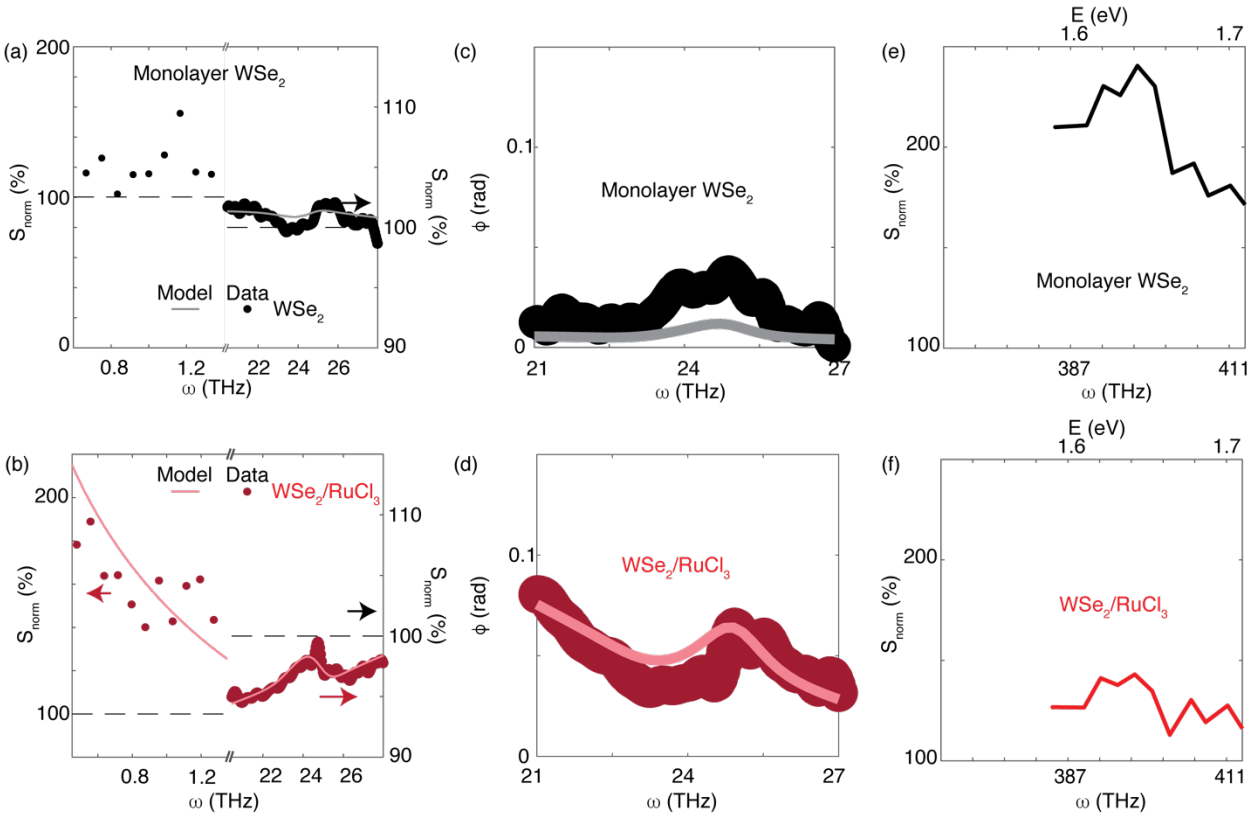

Figure S1. (a,b,e,f) Near-field amplitude, S_{norm}, spectra from THz to Visible frequencies normalized to the SiO_2 substrate. (a) THz and Mid-infrared amplitude spectra on a monolayer WSe_2. (c) THz and Mid-infrared amplitude spectra on $WSe_2/RuCl_3$. (c) Mid-IR phase spectra on monolayer WSe_2. (d) Mid-IR phase spectra on $WSe_2/RuCl_3$. The solid lines are calculated with the lightning rod model (see text for parameters). (e) Visible spectra on monolayer WSe_2. (f) Visible spectra on $WSe_2/RuCl_3$.

To fit the experimental spectra, we constructed the dielectric tensor of each layer with a Drude-Lorentz model:

$$\varepsilon_I^i = \varepsilon_{\infty,I}^i - \frac{\omega_{p,I}^i}{\omega^2 + i\omega\gamma_{D,I}^i} + \frac{N_{eff}^{i\,2}\Omega_I^{i\,2}}{\omega_{TO,I}^{i\,2} - \omega^2 - i\omega\gamma_I^i} \qquad \text{(S1)}$$

The parameters are given in Table S1. The superscript, i, is used to denote the crystal direction (c=[001], b=[010], or a=[100]) while the subscript, I, is used to denote the layer (WSe_2, $RuCl_3$ or SiO_2 in table S1). The near-field amplitude and phase were calculated with the lightning rod

model[2] for a series of trial parameters, $\omega_{p,Wse2}^{a,b}$ and $\gamma_{D,Wse2}^{a,b}$. In the main text we quote the mean-value and use the 95% confidence intervals to calculate the error-bars.

As we remark in the main text the assumption that $RuCl_3$ and WSe_2 are doped with the same carrier density yields $\omega_{p,RuCl3}^{a,b,c} = \sqrt{\frac{m_{WSe2}^*}{m_{RuCl3}^*}}\,\omega_{p,Wse2}^{a,b,c}$. Reported values of the hole mass of WSe_2 are distributed in the range of about $m_{WSe2}^* \approx 0.3 - 0.5\, m_e$ [3-5]. We use the mean value $m_{WSe2}^* \approx 0.4\, m_e$ to estimate the carrier density with Eq. (S2) below. We remark that the error bars for the density also includes the spread of values for the effective mass found in the literature. In our model we assume only the top layer of $RuCl_3$ is doped. The Drude scattering rate of $RuCl_3$ is set to $\gamma_{D,RuCl3}^{a,b,c} = 500\ cm^{-1}$. We checked a few values of $\gamma_{D,RuCl3}^{a,b,c}$ and found that our results are insensitive to the exact value of $\gamma_{D,RuCl3}^{a,b,c}$ if it remains within a reasonable range of ~100-1000 cm^{-1}. We, further, took the plasma-frequency to be zero along the c-axis of WSe_2 owing to the high-effective mass anisotropy[6]. Given the slight thickness of the WSe_2 monolayer our results are also insensitive to the exact choice of the c-axis plasma frequency. We remark that the possible slight doping of the next few layers of $RuCl_3$ also has a negligible on the spectrum in our model, as the associated spectral weight is suppressed by the large effective mass of $RuCl_3$, approximately equal to the vacuum free electron mass[7]. We also tested the extreme assumption that RuCl3 is not doped at all: $\omega_{p,RuCl3}^{a,b,c} = 0$. The same procedure described in the above paragraph then yields these values for WSe_2: $\omega_p = \omega_p = 5{,}300\ (+/-400)\ cm^{-1}$ and $\gamma = 330\ (+/-\ 60)\ \ cm^{-1}$. Note that these values are within the

error-bars of the values quoted within the main text, further supporting the notion that details of the spectral weight of $RuCl_3$ can be neglected.

To estimate the carrier density, we used the formula:

$$n = d(0.724\ x\ 10^{21}\ cm^{-3})\left(\frac{m^*_{WSe2}}{m_e}\right)\left(\frac{\hbar\omega_p}{8065.6}\right)^2 \qquad \text{(S2)}$$

Where d = 0.65 nm is the thickness of WSe_2.

Table S1: Parameters used in our fitting. The value of N_{eff} = 1 is used to model all low energy (mid-IR and THz) data. See text and Fig. S2 for the parameters used to model the A-exciton resonance in WSe_2.

	SiO_2	$RuCl_3$	WSe_2
$\varepsilon_\infty^{[001]}$	1.96	6.2	3.8
Ω_I^i	89 [cm^{-1}]	2222 [cm^{-1}]	-
$\omega_{TO}^{[001]}$	808 [cm^{-1}]	753.9 [cm^{-1}]	-
$\gamma^{[001]}$	32 [cm^{-1}]	941.7 [cm^{-1}]	-
$\varepsilon_\infty^{[010]}$	1.96	6.2	12.3
$\omega_{LO}^{[010]}$	89 [cm^{-1}]	2222 [cm^{-1}]	-
$\omega_{TO}^{[010]}$	808 [cm^{-1}]	753.9 [cm^{-1}]	-
$\gamma^{[010]}$	32 [cm^{-1}]	941.7 [cm^{-1}]	-
$\varepsilon_\infty^{[100]}$	1.96 [ref]	6.2	12.3
$\omega_{LO}^{[100]}$	89 [cm^{-1}]	2222 [cm^{-1}]	-
$\omega_{TO}^{[100]}$	808 [cm^{-1}]	753.9 [cm^{-1}]	-
$\gamma^{[100]}$	32 [cm^{-1}]	941.7 [cm^{-1}]	-
d	285 [nm]	7 [nm]	0.65 [nm]

The A-exciton resonance was modeled with the Lorentz model (Eq. (S1)) for WSe_2 and $WSe_2/RuCl_3$. In this model the oscillator strength is given in arbitrary units. The value of the oscillator strength is scaled with the coefficient N_{eff} in Eq. (S1). The other parameters extracted from the data set shown in Fig. 4 of the main text are shown below in Fig. S2. A systematic suppression of the oscillator strength correlates with the topographic height, while only minor

changes of the other parameters appearing in Eq. (S1) were detected. It is possible that the slight shift in the center frequency of the A-exciton resonance, ω_{TO}, could be impacted by strain and other effects, in addition to changes of the carrier density. Note that below a height of around 15 nm a reliable fit of the data was not possible due to the suppressed oscillator strength reported in Fig. 4 of the main text. Thus, values for ω_{TO} and γ are not reported in Fig. S2 below this height.

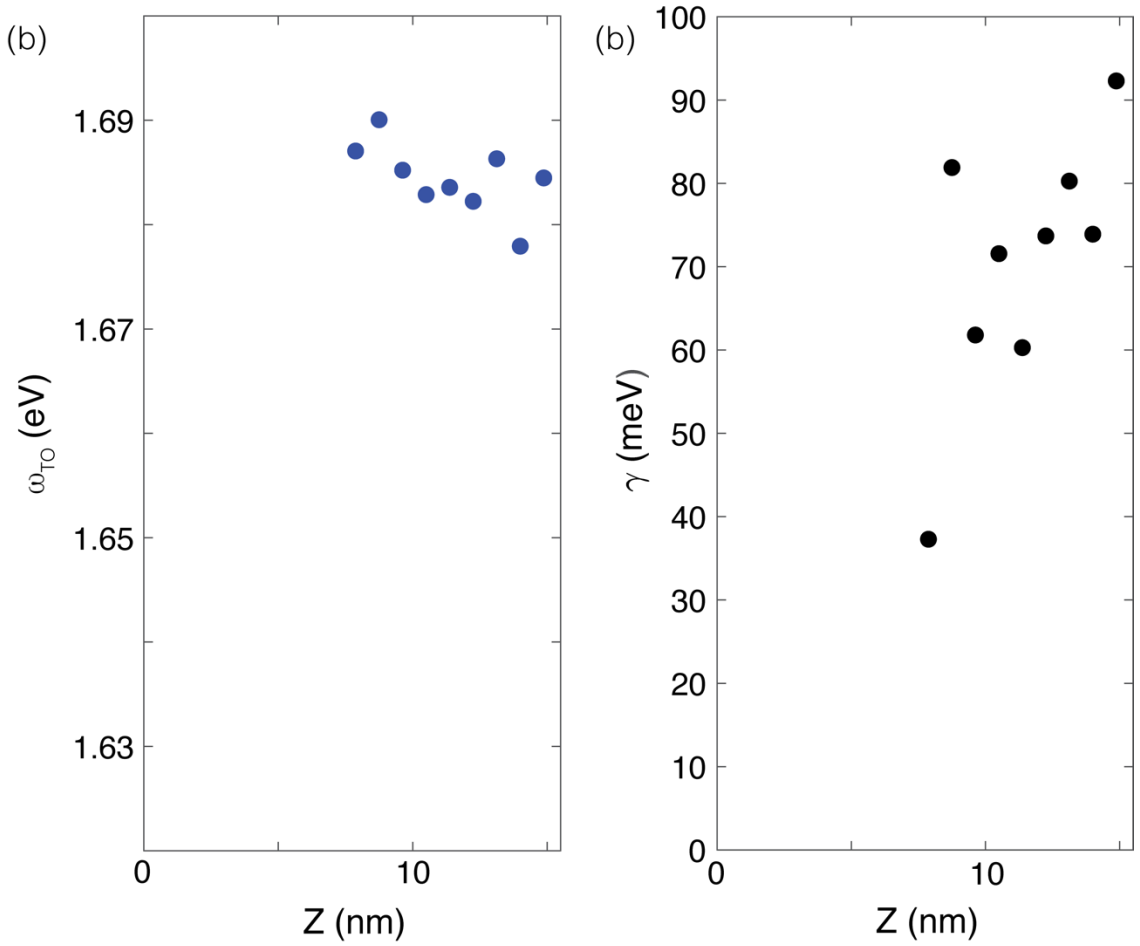

Figure S2. Parameters of the Lorentz model for spectra on a nanobubble in the $WSe_2/RuCl_3$ heterostructure.

Section 1.2 - DFT calculations

The ab initio calculations were performed within the Vienna Ab initio Simulation Package (VASP)[8] using a projector-augmented wave (PAW) pseudopotential in conjunction with the Perdew–Burke–Ernzerhof (PBE)[9] functionals and plane-wave basis set with energy cutoff at 400 eV. For the heterostructures with WSe_2 and monolayer α-$RuCl_3$, we used a hexagonal supercell containing 275 atoms (composed of a 7×7 WSe_2 supercell and 4×4 α-$RuCl_3$ supercell). The resulting strain is ~3.5% for the WSe_2 monolayer. The surface Brillouin zone was sampled by a 3 × 3 × 1 Monkhorst–Pack k-mesh. A vacuum region of 15 Å was applied to avoid artificial interaction between the periodic images along the z direction. Due to the absence of strong chemical bonding between layers, van der Waals density functional in the opt88 form[10] was employed for structural optimization. All structures were fully relaxed until the force on each atom was less than 0.01 eV $Å^{-1}$. Spin-orbital couplings are included in the electronic calculations.

The Hubbard U terms are computed by employing the generalized Kohn–Sham equations within density functional theory including mean-field interactions, as provided by the Octopus package,[11, 12] using the ACBN0[13, 14] functional together with the local density approximation (LDA) functional describing the semilocal DFT part. We compute ab initio the Hubbard U and Hund's J for the 4d orbitals of Ruthenium and 3p orbital of Chlorine. We employ norm-conserving HGH pseudopotentials to get converged effective Hubbard U values (1.96 eV for Ru 4d orbitals and 5.31 eV for Cl 3p orbitals) with spin-orbital couplings.

We inquire into the physical mechanism of charge transfer through DFT calculations on model WSe_2/α-$RuCl_3$ heterostructures. A bandgap of 0.86 eV is observed in the calculated band structure of monolayer α-$RuCl_3$ in Fig. S2a is in good agreement with the experimental observations[15]. The bandgap of pristine monolayer WSe_2 is calculated to be around 1.2 eV from DFT calculations.

We used first-principles calculations to explore the electronic structure of the heterostructure (Figure S3). The charge transfer at the interface is important to understand the interface-modified electronic structures. We obtain that the charge transfer from WSe_2 to $RuCl_3$ is 0.20 electrons in the simulated supercell, corresponding to electron doping with the density concentration of n = 3.95x10^{12} cm^{-2} in the $RuCl_3$ layer.

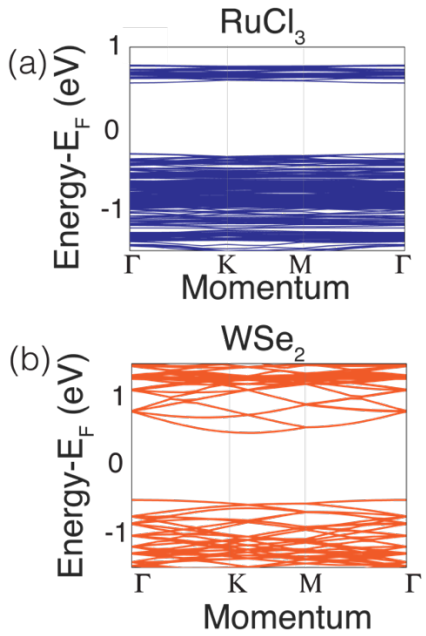

Figure S3. Supplementary calculations. (a) DFT band structure of $RuCl_3$. (b) DFT band structure of WSe_2.

Supporting References:

1. Zhang, S.; Li, B.; Chen, X.; Ruta, F. L.; Shao, Y.; Sternbach, A. J.; McLeod, A. S.; Sun, Z.; Xiong, L.; Moore, S. L.; Xu, X.; Wu, W.; Shabani, S.; Zhou, L.; Wang, Z.; Mooshammer, F.; Ray, E.; Wilson, N.; Schuck, P. J.; Dean, C. R.; Pasupathy, A. N.; Lipson, M.; Xu, X.; Zhu, X.; Millis, A. J.; Liu, M.; Hone, J. C.; Basov, D. N. Nano-spectroscopy of excitons in atomically thin transition metal dichalcogenides. *Nature Communications* **2022,** 13, (1), 542.
2. McLeod, A. S.; Kelly, P.; Goldflam, M. D.; Gainsforth, Z.; Westphal, A. J.; Dominguez, G.; Thiemens, M. H.; Fogler, M. M.; Basov, D. N. Model for quantitative tip-enhanced spectroscopy and the extraction of nanoscale-resolved optical constants. *Physical Review B* **2014,** 90, (8), 085136.
3. Fallahazad, B.; Movva, H. C. P.; Kim, K.; Larentis, S.; Taniguchi, T.; Watanabe, K.; Banerjee, S. K.; Tutuc, E. Shubnikov--de Haas Oscillations of High-Mobility Holes in Monolayer and Bilayer WSe2: Landau Level Degeneracy, Effective Mass, and Negative Compressibility. *Physical Review Letters* **2016,** 116, (8), 086601.
4. Conti, S.; Neilson, D.; Peeters, F. M.; Perali, A., Transition Metal Dichalcogenides as Strategy for High Temperature Electron-Hole Superfluidity. In *Condensed Matter*, 2020; Vol. 5.
5. Zhao, W.; Ribeiro, R. M.; Toh, M.; Carvalho, A.; Kloc, C.; Castro Neto, A. H.; Eda, G. Origin of Indirect Optical Transitions in Few-Layer MoS2, WS2, and WSe2. *Nano Letters* **2013,** 13, (11), 5627-5634.
6. Sternbach, A. J.; Chae, S. H.; Latini, S.; Rikhter, A. A.; Shao, Y.; Li, B.; Rhodes, D.; Kim, B.; Schuck, P. J.; Xu, X.; Zhu, X. Y.; Averitt, R. D.; Hone, J.; Fogler, M. M.; Rubio, A.; Basov, D. N. Programmable hyperbolic polaritons in van der Waals semiconductors. *Science* **2021,** 371, (6529), 617.
7. Rizzo, D. J.; Jessen, B. S.; Sun, Z.; Ruta, F. L.; Zhang, J.; Yan, J.-Q.; Xian, L.; McLeod, A. S.; Berkowitz, M. E.; Watanabe, K.; Taniguchi, T.; Nagler, S. E.; Mandrus, D. G.; Rubio, A.; Fogler, M. M.; Millis, A. J.; Hone, J. C.; Dean, C. R.; Basov, D. N. Charge-Transfer Plasmon Polaritons at Graphene/α-RuCl3 Interfaces. *Nano Letters* **2020,** 20, (12), 8438-8445.
8. Kresse, G.; Furthmüller, J. Efficient iterative schemes for ab initio total-energy calculations using a plane-wave basis set. *Physical Review B* **1996,** 54, (16), 11169-11186.
9. Perdew, J. P.; Burke, K.; Ernzerhof, M. Generalized Gradient Approximation Made Simple. *Phys Rev Lett* **1996,** 77, (18), 3865-3868.
10. Klimeš, J.; Bowler, D. R.; Michaelides, A. Van der Waals density functionals applied to solids. *Physical Review B* **2011,** 83, (19), 195131.
11. Andrade, X.; Strubbe, D.; De Giovannini, U.; Larsen, A. H.; Oliveira, M. J. T.; Alberdi-Rodriguez, J.; Varas, A.; Theophilou, I.; Helbig, N.; Verstraete, M. J.; Stella, L.; Nogueira, F.; Aspuru-Guzik, A.; Castro, A.; Marques, M. A. L.; Rubio, A. Real-space grids and the Octopus code as tools for the development of new simulation approaches for electronic systems. *Physical Chemistry Chemical Physics* **2015,** 17, (47), 31371-31396.
12. Tancogne-Dejean, N.; Oliveira, M. J. T.; Andrade, X.; Appel, H.; Borca, C. H.; Le Breton, G.; Buchholz, F.; Castro, A.; Corni, S.; Correa, A. A.; De Giovannini, U.; Delgado, A.; Eich, F. G.; Flick, J.; Gil, G.; Gomez, A.; Helbig, N.; Hübener, H.; Jestädt, R.; Jornet-Somoza, J.; Larsen, A. H.; Lebedeva, I. V.; Lüders, M.; Marques, M. A. L.; Ohlmann, S. T.; Pipolo, S.; Rampp, M.; Rozzi, C. A.; Strubbe, D. A.; Sato, S. A.; Schäfer, C.; Theophilou, I.; Welden, A.; Rubio, A. Octopus, a

computational framework for exploring light-driven phenomena and quantum dynamics in extended and finite systems. *The Journal of Chemical Physics* **2020,** 152, (12), 124119.
13. Tancogne-Dejean, N.; Oliveira, M. J. T.; Rubio, A. Self-consistent DFT+U method for real-space time-dependent density functional theory calculations. *Physical Review B* **2017,** 96, (24), 245133.
14. Agapito, L. A.; Curtarolo, S.; Buongiorno Nardelli, M. Reformulation of DFT+U as a Pseudohybrid Hubbard Density Functional for Accelerated Materials Discovery. *Physical Review X* **2015,** 5, (1), 011006.
15. Zhou, X.; Li, H.; Waugh, J. A.; Parham, S.; Kim, H.-S.; Sears, J. A.; Gomes, A.; Kee, H.-Y.; Kim, Y.-J.; Dessau, D. S. Angle-resolved photoemission study of the Kitaev candidate α-RuCl3. *Physical Review B* **2016,** 94, (16), 161106.